Three-dimensional graphene network assisted high performance dye sensitized solar cells

Bo Tang [a], Guoxin Hu [a,*], Hanyang Gao [b], Zixing Shi [c]

[a] School of Mechanical and Power Engineering, Shanghai Jiaotong University, No. 800 Dongchuan Road, Shanghai 200240, China
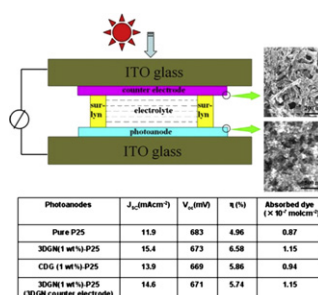[b] School of Environmental Science and Engineering, Shanghai Jiaotong University, No. 800 Dongchuan Road, Shanghai 200240, China
[c] School of Chemistry and Chemical Engineering, Shanghai Jiaotong University, No. 800 Dongchuan Road, Shanghai 200240, China

HIGHLIGHTS

► Three-dimensional graphene network (3DGN) is prepared on Ni foam by CVD for DSSCs.
► The fabricated 3DGN possesses large BET area and high electrode conductivity.
► The η is 6.58% for 3DGN modified DSSC, which is 32% higher than P25 based one.
► A high performance DSSC with 3DGN based photoanode and counter electrode is made.

GRAPHICAL ABSTRACT

Photoanodes	J_{sc} (mAcm²)	V_{oc} (mV)	η (%)	Absorbed dye ($\times 10^{-7}$ molcm⁻²)
Pure P25	11.9	683	4.96	0.87
3DGN(1 wt%)-P25	15.4	673	6.58	1.15
CDG (1 wt%)-P25	13.9	669	5.86	0.94
3DGN(1 wt%)-P25 (3DGN counter electrode)	14.6	671	5.74	1.15

ARTICLE INFO

ABSTRACT

Three-dimensional graphene networks (3DGNs) are prepared by chemical vapor deposition with the nickel foam rod as a template. Continuous structure of the 3DGN efficiently reduces inter-sheet junction contact resistance between the graphene sheets and makes the sample a great channel for carrier transport. The as-prepared 3DGN is added into the photoanode to boost the photovoltaic performance of dye sensitized solar cells (DSSCs). Even the amount of the 3DGN is as low as 0.2 wt%, the short-circuit current density and power conversion efficiency (η) are obviously improved, which is due to the enhanced dye absorption amount and prolonged electron lifetime. Compared to that of pure P25 photoanode based DSSC, the η increases 32.7% under AM-1.5G one sun light intensity when the 3DGN (1 wt %)−P25 photoanode is adopted (from 4.96% to 6.58%). After optimizing the thickness of the added 3DGN, the η further increases to 6.87%. Moreover, DSSCs with the 3DGN based counter electrode are also fabricated, and a slight degradation (in η) is obtained in comparing with that of employing a Pt counter electrode under identical conditions.

1. Introduction

Solar energy has been regarded as a potential candidate to replace fossil fuels in the further due to its free and inexhaustible features, and dye-sensitized solar cells (DSSCs) have attracted intense interest after the breakthrough in 1991 [1]. Three parts are included in a typical DSSC: counter electrode, photoanode and electrolyte. Pt is always used as the counter electrode material due to its high electrical conductivity, outstanding catalytic property and great stability. However, both the pure Pt and its compounds are rare and expensive. Thereby, developing a high-performance counter electrode material with proper price is important to the widespread use of the DSSCs. On the other hand, P25, as a traditional photoanode material, possesses nice dye absorption property and relatively low recombination rate of the electron−hole pairs, but suffers from

* Corresponding author. Tel./fax: +86 21 34206569.
  E-mail address: hugx@sjtu.edu.cn (G. Hu).

drawbacks of the poor scattering ability and low electrical conductivity. In order to enhance the power conversion efficiency (η) of the DSSCs, several attempts on boosting the electrode performance have been made. Adding a scattering layer outside the P25 film is one of the useful approaches to improve the scattering ability of the photoanode [2,3]. The addition of graphite, carbon nanotubes, carbon hollow spheres and carbon black into the P25 film can obviously enhance the electron transport ability of the photoanode [4–6]. Similarly, these carbon materials also can be employed as the counter electrode to replace the expensive Pt electrode because of their great conductivity, high stability and low cost [7–12].

Graphene, a severe two-dimensional material with SP^2 bonded carbon atoms, has attracted much attention due to its extraordinary electrical and optical properties, large BET area and atomic-scale thickness [13]. Recently, graphene is anticipated as a potential candidate to heighten the dye absorption and carrier transport abilities and hence the η of the DSSCs. Gao et al. adopted graphene–TiO$_2$ (0.5 wt% graphene) to fabricate the photoanode for DSSCs, and the obtained η is much higher than that of the pure TiO$_2$ photoanode based sample [12]. Chen et al. reported graphene assisted P25 photoanode and obtained a 15% increase for the η [14]. Our group prepared DSSCs with a graphene modified photoanode, and the η as high as ~9% [2]. Besides the applications in the photoanode, the graphene can be used as the counter electrode, as well. Jeon and co-workers prepared DSSCs by using a graphene counter electrode, and the η reached 5.69% [15]. Although graphene modified DSSCs have been reported, the employed graphene, without exception, is chemically derived graphene (CDG). It is well-known that the CDG shows high inter-sheet junction contact resistance and poor electrical conductivity owing to severe structural defects in graphene sheets introduced during exfoliation and reduction processes [16]. Moreover, the universal agglomeration of the CDG seriously influences its BET area as well as dye absorption ability [17]. Compared to that of the CDG, the carrier mobility and BET area of the graphene prepared by chemical vapor deposition (CVD) are much better. Recently, Chen's group fabricated three-dimensional graphene networks (3DGN) on a Ni foam template by CVD [16]. Electrical conductivity of the 3DGN assisted poly dimethyl siloxane is ~6 orders of magnitude higher than that of the CDG modified composites. Furthermore, the 3DGN copies the porous structure of the Ni template and possesses a great BET area. Therefore, the 3DGN may be a promising material to further improve the photovoltaic property of the DSSCs.

In this study, we prepared the 3DGN by CVD with Ni foam rods (NFR) as a template, and the 3DGN was added into the photoanode to fabricate high-performance DSSCs. The amounts of the 3DGN in the photoanode range from 0.2 to 2 wt%, and the η of the as-prepared DSSCs obviously increased, which is due to the outstanding electron transport property and great BET area of the 3DGN. Among them, the DSSC with a 1 wt% 3DGN included photoanode showed best photovoltaic performance, and the increases up to 29.4% and 32.7% for the short circuit current density (J_{sc}) and η, respectively. Due to the properties of the 3DGN are closely related to its thickness, we further optimized the 3DGN thickness to improve the performance of the DSSCs, and a η up to 6.87% was obtained. Moreover, the 3DGN was also adopted as the counter electrode material. The resulted DSSCs with the 3DGN based photoanode and counter electrode displayed relatively high photovoltaic performances, demonstrating a hopeful prospect of the 3DGN in the DSSCs area.

2. Experimental

2.1. Reagents and materials

P25 was purchased from Degussa. Acetonitrile and polytetrafluoroethylene were obtained commercially from the Beijing chemical reagent plant (Beijing, China). Chloroplatinic acid, poly(-methyl methacrylate) (PMMA), indoline, iodine and potassium iodide were purchased from Aladdin Co. Polytetrafluoroethylene (PTFE) was purchased from the Shanghai Deyuan industrial Co., Ltd. Deionized water (resistivity 18 MΩ cm) was utilized to prepare all aqueous solutions. The P25 was heated at 500 °C for 2 h to remove the organics and dust for the subsequent experiments.

2.2. Preparation of 3DGN and CDG

The NFR was heated to 1100 °C under the Ar (300 sccm) and H$_2$ (150 sccm) conditions with a 20 °C min^{-1} heating rate. After annealing for 20 min, a small amount of CH$_4$ was introduced (25 sccm). After 10 min for graphene growth, the sample was cooled down to room temperature under H$_2$ and Ar conditions. In order to obtain free-standing 3DGN, the NFR was removed by HCl (1 mol L^{-1}) solution at 76 °C for 6 h. It is worth to note that a thin PMMA (average molecular mass 996,000, 4% in ethyl lactate) was used as a support to remain the foam structure of the graphene network before the corrosion process. Finally, the free-standing 3DGNs were obtained by dissolving the PMMA in hot acetone at 60 °C. The preparation of the CDG was according to recent report [18].

2.3. Preparation of electrodes

3DGN–P25 photoanode: The conductive glass was cleaned by propanol with an ultrasonic bath for 1 h and then rinsed with deionized water. 3DGN was mixed with P25 (0.2, 0.5, 1, 2 wt%) and then the mixture was moved to an ethanol solution for supersonic treatment (5 min). Afterward, the obtained paste was deposited on the conductive glass by doctor-blade method, and the as-prepared sample was heated to 300 °C under Ar atmosphere and kept 30 min. *CDG–P25 photoanode*: The fabrication process is similar with the 3DGN–P25 photoanode. *Pt counter electrode*: The process is according to our previous paper [2]. *3DGN counter electrode*: 0.02 g 3DGN was mixed with PTFE (4 wt%) and then deposited to the conductive glass by doctor-blade method.

2.4. Characterization

X-ray diffraction (XRD) analysis was recorded on Bruker D8 Advance using Cu Kα radiation ($\lambda = 0.154$ nm). The morphology images were carried out by transmission electron microscopy (TEM) (JEM-2100F operated at an accelerating voltage of 20kv). Raman spectra were performed by LabRam-1B Raman microspectrometer at 514.5 nm (Horiba Jobin Yvon, France). The Brunauer–Emmett–Teller (BET) surface areas were measured on a Nova 100 by using N$_2$ as the adsorption gas. Atomic Force Microscopy (AFM) results were recorded by E-Sweep (Seiko, Japan) in tapping mode. Scanning electron microscope (SEM) images were obtained by FEI Sirion 200 scanning electron microscope working at 5 kV. Photocurrent measurements and electrochemical impedance spectroscopy (EIS) were performed on a CHI 660D electrochemical analyzer (Shanghai CH Instrument Company, China). X-ray photoelectron spectroscopy (XPS) measurements were performed on AXIS Ultra DLD (Kratos). Fourier transform infrared spectroscopy (FTIR) curves were measured on IR Prestige-21 system (PerkinElmer).

2.5. Preparation and measurement of DSSCs

The detailed preparation of the DSSCs is according to the previous report [2]. The J–V curves were recorded by a PGSTAT 30 potentiostat (Netherlands). The incident photon-to-current conversion efficiency (IPCE) profiles were recorded on a Newport 1918-c power meter.

3. Results and discussion

3.1. Characterization of the samples

SEM images of the as-prepared 3DGN with and without NFR template are shown in Fig. 1a. The free-standing 3DGN (inset of Fig. 1a) copies the 3D morphology of the NFR (see Fig. S1), which efficiently reduces the inter-sheet junction contact resistance between the graphene sheets. Moreover, the continuous 3D structure endows the 3DGN a great electron transport channel to bridge the conductive glass substrate and P25. No obvious distinction can be seen for the 3DGN with varied thicknesses (Fig. 1b and the inset in the right-side show mono- and three-layer 3DGNs, and Fig. S2 displays the bi-layer sample). The resulted wrinkles and ripples result from the difference between the thermal expansion coefficients of the nickel and graphene [19]. High magnification cross-section TEM images clearly reveal the mono- and three-layer feature (inset in the left-side of Fig. 1b) of the sample, and few thicker 3DGN can be found (>10 layers) in the end-point area of the NFR (see Fig. S3). Due to the NFR template parallels with the CH$_4$ gas flow during the 3DGN growth, varied concentration gradients of the CH$_4$ gas along the NFR axis direction provide necessary condition to grow the 3DGN with different thicknesses in one substrate simultaneously (thickness of the 3DGN decreases along the axis direction of the NFR template, see inset of Fig. 1c).

The corresponding Raman curves of the 3DGN with mono-, bi- and multi-layers are shown in Fig. 1c. All curves display intense G and 2D peaks and weak D peak, indicating the high quality of the prepared specimens [20]. The numbers of layers of the 3DGN are identified by the profile of the 2D peak and intensity ratio of the 2D peak to G peak [21–24]. According to the double-resonant Raman model, the profile of the 2D peak is closely related to the thickness of the graphene [25]. Briefly, due to the splitting of the electronic bands, the 2D peak of the multilayer graphene splits to some Lorentzian components (more details see Supporting Information and Fig. S4). The peak can be fitted by a single Lorentzian component for the monolayer sample, while 4 Lorentzian components are needed to reproduce the 2D peak of the bi-layer sample [20]. With the further increased thickness of the graphene, the needed Lorentzian components decrease to two to fit the corresponding 2D band. The detailed fitting of the 2D band from the 3DGN with varied thicknesses is displayed in the inset of Fig. 1c. Moreover, the full width at half maximum (FWHM) of the 2D peak increases to ~56 cm^{-1} for the bi-layer 3DGN from ~27 cm^{-1} for the monolayer one, and then increases to ~63 cm^{-1} when the number of layers is larger than three, which is similar with the plane two-dimensional graphene [21,26]. Correspondingly, the value of I_{2D}/I_G gradually reduces with the increased thickness [27–29]. Fig. 1d displaces AFM images of the monolayer and three-layer 3DGN (removing the NFR by 1 mol L^{-1} HCl solution). The large-scale monolayer 3DGN partly maintains the morphology of the NFR (the unfolded foam structure), which is consistent with the SEM images. XRD patterns of the free-standing 3DGN are shown in Fig. S5. A weak peak indexed as
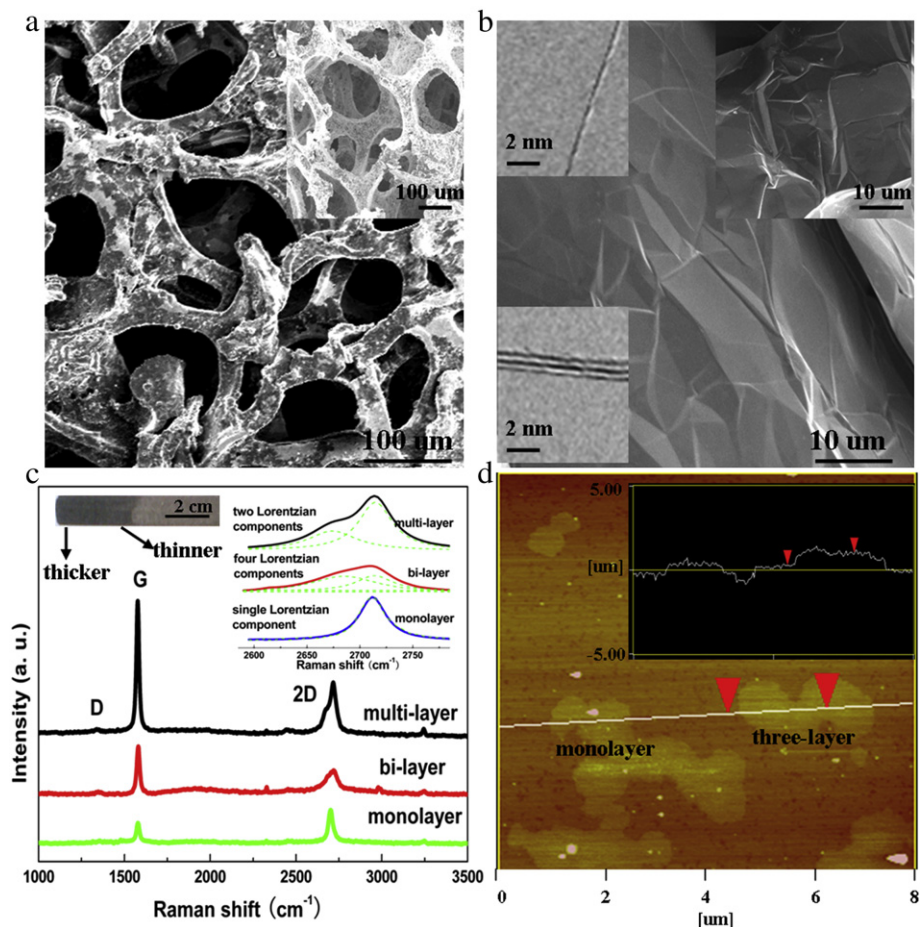
Fig. 1. (a) SEM image of the 3DGN with NFR template, and the inset shows the free-standing 3DGN; (b) SEM image of the monolayer 3DGN, insets demonstrate SEM of the three-layer 3DGN and cross-sectional TEM images of the monolayer and three-layer 3DGN; (c) Raman curves of the monolayer, bi-layer and few-layer 3DGN, and the inset displays the detailed image of 2D peaks and the digital image of the NFR; (d) AFM image of the monolayer and three-layer 3DGN.

(002) diffraction planes of carbon-like materials can be seen from the three-layer and thicker samples [30], and detailed image of the peak is displayed as the inset.

Fig. 2a presents SEM image of the P25, which possesses porous surface and uniform particle size about ∼40 nm. After adding the 3DGN with varied amounts, the P25 exhibits similar rough surface but a larger pore appearance (Fig. 2b–d), demonstrating that the 3DGN is a great carrier for the P25 [18]. The presence of the 3DGN improves the BET area of the photoanode (see Table 1). Therefore, the 3DGN is expected to not only play as the transport channel for the photogenerated electrons but also enhance the dye absorption ability of the photoanode. The performances of the photoanode depend heavily on the interface state between the 3DGN and P25, which should be further analyzed. Fig. 3a shows the cross-section SEM image of the as-prepared 3DGN, and the laminated structure of the graphene sheets can be seen clearly. After mixing with P25, the P25 nanoparticles cover the surface of the 3DGN (see Fig. 3b). Due to the amount of the 3DGN in the photoanode is small (1 wt%), it is difficult to find the entire naked 3DGN. In the high magnification SEM image, the 3DGN can be found from the margin area (Fig. 3c, d). In order to further analyze the interface between the 3DGN and P25, FTIR of the 3DGN, P25 and the 3DGN (1 wt%)–P25 was recorded. As shown in Fig. S6, the absorption band located at 1600 cm^{-1} is assigned to the skeletal vibration of the graphene sheets, while the low-frequency absorption below 1000 cm^{-1} is attributed to the Ti–O–Ti vibration of the P25 [31]. Moreover, the

absorption peak results from the O–H stretching vibration of the surface hydroxyl from adsorbed water located at 3400 cm^{-1} [32]. No obvious change or new peak can be found from the curve of the 3DGN (1 wt%)–P25, demonstrating no chemical interaction existence between the 3DGN and P25. Based on our recent paper [18], the absorption band below 1000 cm^{-1} would become wider when a chemical bond forms between the graphene and TiO$_2$ materials. Due to the 3DGN (1 wt%)–P25 was prepared by physical mixing, no chemical bond existence between them is reasonable.

3.2. Performance of DSSCs

The J–V curves of the DSSCs with the pure P25 and 3DGN–P25 photoanodes are shown in Fig. 4a. The J_{sc} and η of the P25 photoanode based DSSCs are 11.9 mA cm^{-2} and 4.96%, respectively. After adding the 3DGN into the photoanode, obvious increases in both the J_{sc} and η can be seen (see Table 1 and Fig. 4a). Although the 3DGN absorbs a small part of incident light, the presence of this material in the DSSCs is positive due to its large BET area (absorbing more dye molecules) and outstanding electrical property (acting as the electron transport channel). Moreover, considering the high transmittance of the graphene [33], the 3DGN is benefit for the DSSCs when its mass ratio is less than a critical amount in the photoanode (more detailed analysis in Supporting Information and Figs. S7, S8). Among these 3DGN assisted specimens, the DSSCs with 1 wt% 3DGN included photoanode show best photovoltaic
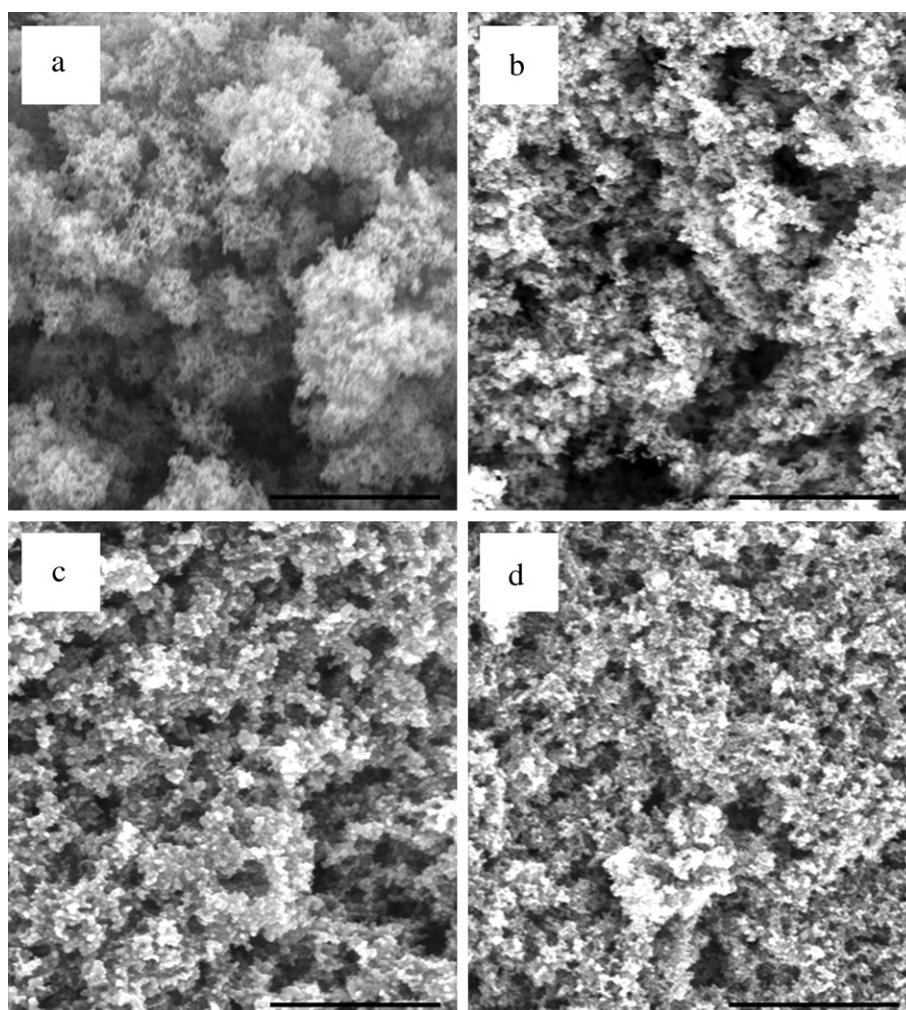

Fig. 2. SEM images of the (a) pure P25; (b) 3DGN (0.5 wt%)–P25; (c) 3DGN (1 wt%)–P25; (d) 3DGN (2 wt%)–P25; the scale bar represents 500 nm.

Table 1
Results of photovoltaic properties and dye loading of the DSSCs with varied photoanodes (thickness is 10 μm) and counter electrode. All measurements were recorded under AM-1.5G one sun and the active areas were ca. 0.15 cm^2 for all cells.

Photoanodes	J_{sc} (mA cm^{-2})	V_{oc} (mV)	FF (%)	η (%)	Absorbed dye ($\times 10^{-7}$ mol cm^{-2})	BET area (m^3 g^{-1})
Pure P25	11.9	683	61.0	4.96	0.87	49.757
3DGN (0.2 wt%)–P25	12.4	676	62.2	5.21	0.92	67.954
3DGN (0.5 wt%)–P25	13.6	671	63.4	5.79	1.03	92.387
3DGN (1 wt%)–P25	15.4	673	63.5	6.58	1.15	117.658
3DGN (2 wt%)–P25	14.1	674	63.2	6.01	1.28	182.753
CDG (1 wt%)–P25	13.9	669	63.1	5.86	0.94	66.524
3DGN (1 wt%)–P25 (3DGN counter electrode)	14.6	671	58.6	5.74	1.15	117.658

characteristics, and the increases for the J_{sc} and η reach 29.4% and 32.7%, manifesting the synergy effect between the 3DGN and P25. Insufficient 3DGN could not provide enough electron transport channels, while more photons are absorbed by excess black 3DGN to generate heat [2,18]. In order to confirm the outstanding property of the 3DGN, a CDG modified DSSC was also fabricated for the purpose of comparison. The photovoltaic performance of the CDG added DSSC (see Table 1) is not as good as the 3DGN assisted samples (η are 5.86% and 6.58%, respectively, both the mass ratio of the CDG and 3DGN in the photoanode is 1 wt%), indicating the better properties of the 3DGN. The IPCE patterns of prepared samples are shown in Fig. 4b, and an increase over the entire wavelength range in the IPCE was obtained for the 3DGN–P25 photoanode built DSSCs. Moreover, photocurrent of the

photoanode increases 500% after adding the 3DGN (inset of Fig. 4b). Based on the above results, it can be found that the 3DGN evidently enhances the electron transport efficiency of the photoanode. On the other hand, the photogenerated electron–hole pairs in the P25 are more efficiently separated in the presence of the 3DGN due to the Fermi level of graphene is more positive than the conduction band of TiO$_2$ (0 V vs NHE for graphene and −0.5 V vs NHE for TiO$_2$) [34]. In addition, considering the P25 nanoparticles coat the 3DGN surface from the SEM images, the photogenerated electrons would rapidly separate and transfer from the P25 to conductive glass through the 3DGN.

In order to further analyze the electron transport in the DSSCs with varied photoanodes, dark currents were recorded. The dark current originates from the reduction of I$_3^-$ ions by the electrons
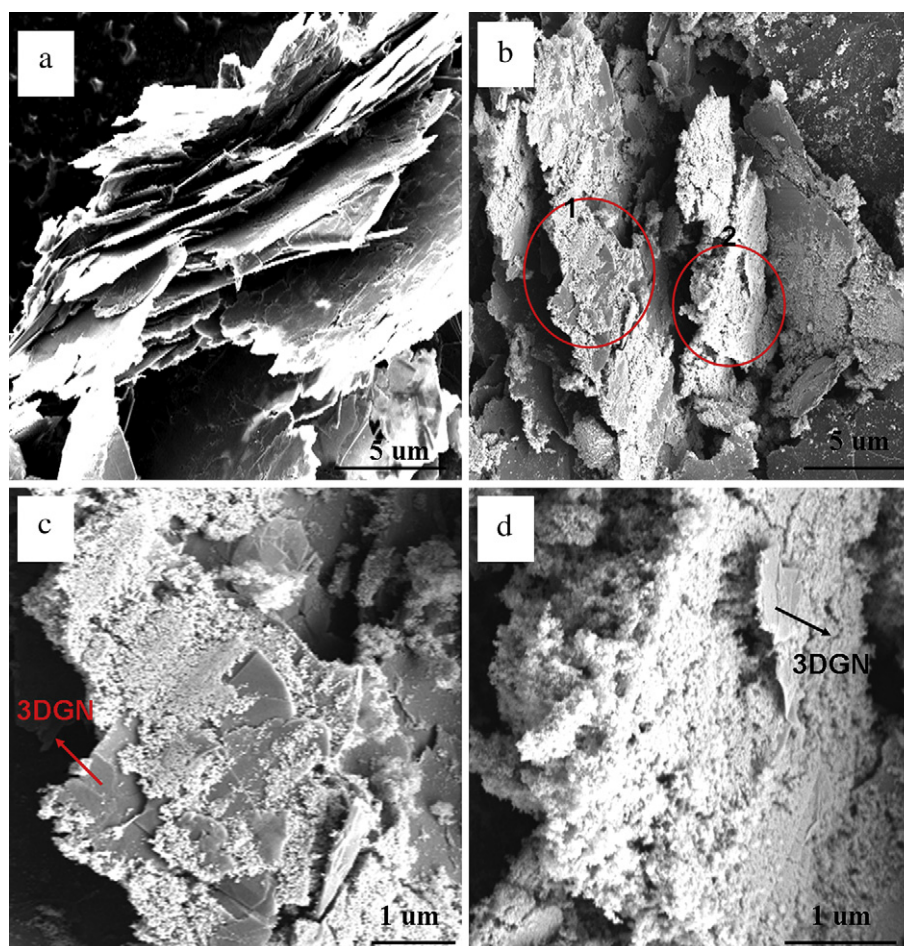
Fig. 3. Cross-section image of the (a) 3DGN; (b) 3DGN (1 wt%)–P25; the high magnification images of the areas in the red circles are shown in the (c) and (d). The exposed 3DGN in the margin is marked. (For interpretation of the references to colour in this figure legend, the reader is referred to the web version of this article.)
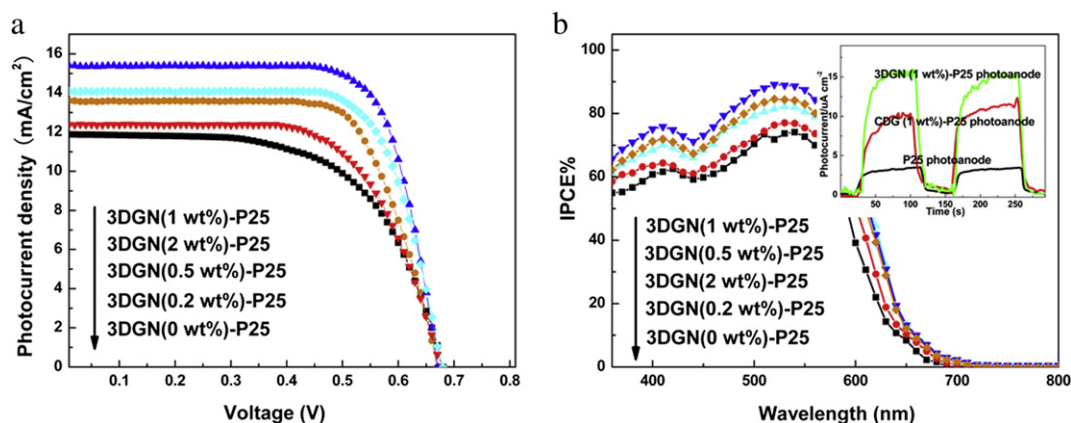
Fig. 4. (a) *J*–*V* curves and (b) IPCE curves of the DSSCs with different photoanodes, the inset shows photocurrent of the pure P25, CDG (1 wt%)–P25 and 3DGN (1 wt%)–P25 photoanodes.

from the conductive glass, which provides a qualitative method to describe the back electron transfer [3,35]. Fig. 5 shows that the dark currents of the 3DGN (1 wt% in the photoanode) assisted DSSCs are smaller than that of the P25 photoanode based sample at the same potential above 0.58 V, and the onset of the dark current shifts to a higher potential (increase by 0.08 V) after adding the 3DGN, indicating a lower combination rate between the photogenerated electron and I_3^- ions in the 3DGN modified sample. Considering the continuous structure of the 3DGN, its inter-sheet junction contact resistance should be far less than that of the CDG. As expected, the CDG modified sample shows a larger dark current, demonstrating the better electrical property of the 3DGN again [16]. Moreover, the photogenerated electron lifetime in the P25, CDG (1 wt%)–P25 and 3DGN (1 wt%)–P25 photoanodes were measured by fluorescence spectrum (inset of Fig. 5). Compared to that of the pure P25 electrode, a longer electron lifetime can be observed in the 3DGN–P25 electrode (extending 25%), which is also longer than that of the CDG (1 wt%)–P25 electrode (extending 9%). Therefore, compared to the CDG, the 3DGN further improves the separation and transport efficiencies of the photogenerated electrons in the photoanode.

Besides the improved electron separation and transport abilities, increased dye absorption amount is another reason for the enhanced photovoltaic performance of the 3DGN modified DSSCs. The dye absorption abilities of the as-prepared photoanodes are summarized in Table 1. Compared to that of the pure P25 photoanode with identical thickness, the presence of the 3DGN significantly increases the amount of dye absorption due to its large BET area. The 2 wt% 3DGN included photoanode displays the highest dye absorption amount, which is 48% higher than that of the pure P25 photoanode. Therefore, both the excellent electron conductivity and large BET area of the 3DGN endow the photoanodes as well as the DSSCs great photovoltaic properties.

The electrochemical impedance spectroscopy (EIS) of the DSSCs with the pure P25, CDG (1 wt%)–P25 and 3DGN (1 wt%)–P25 photoanodes at an applied bias of V_{oc} are shown in Fig. 6. The Z' and Z'' are the real and imaginary parts of the impedance, respectively. In the high-frequency and middle-frequency regions, two semicircles can be seen in all curves. The former reflects the impedance of the charge transfer process at the counter electrode, while the latter is related to the charge transport process at the photoanode–electrolyte interface [12,14,15]. The equivalent circuit of the DSSCs is shown as an inset of Fig. 6. The Z_w, CPE, R_s, R_{ct1} (R_{ct2}) represent Warburg impedance, double-layer capacitance of the interface, series resistance, charge-transfer resistance between electrolyte and counter electrode (photoanode), respectively

[36,37]. After adding the CDG into the photoanode, the semicircle size in the middle-frequency decreases, demonstrating the lower interfacial resistance between the CDG added photoanode and electrolyte. As for the 3DGN modified DSSC, the further decreased height and diameter of the semicircle in the middle-frequency suggest that the 3DGN is more efficient than the CDG to improve the electron transport between the interface of the photoanode and electrolyte. Two reasons lead to the obviously decreased interface resistance. Firstly, the high conductivity of the 3DGN bridges the electrolyte and insulated P25 to promote the electron transport at the interface. Secondly, more photogenerated electrons can reach the conductive glass due to the depressed recombination of electron–hole pairs in the presence of the 3DGN. Moreover, the larger BET area and lower defect density of the 3DGN are the reasons for the better performance compared to that of the CDG. The diameter of the semicircle in the middle-frequency regions reflects the scale of the interfacial impedance [12]. Therefore, the interface impedance between the 3DGN assisted photoanode and electrolyte is far lower than that of the pure P25 (as well as the CDG) based sample, showing the obviously improved interface performance.

The BET area and electrochemical property of the 3DGN are closely related to its thickness. Meanwhile, the photovoltaic performances of the DSSCs depend heavily on the properties of the
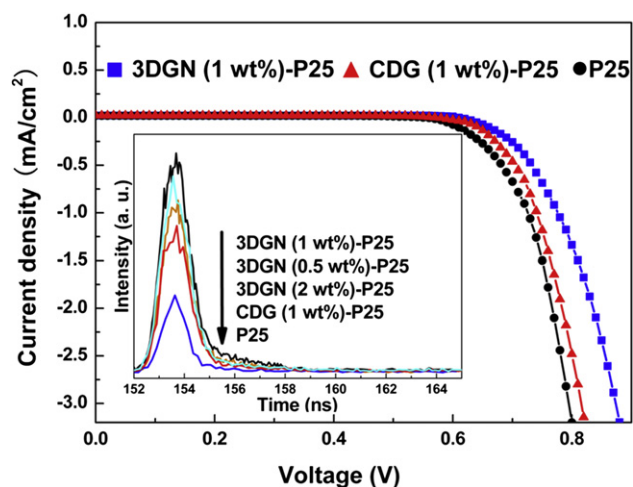
Fig. 5. Dark current of the DSSCs with pure P25, CDG (1 wt%)–P25 and 3DGN (1 wt%)–P25 photoanodes. The inset displays the lifetime of the photogenerated electron in these photoanodes.
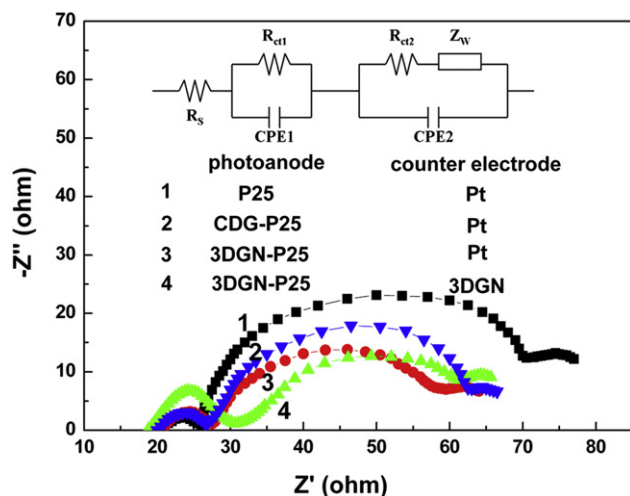
Fig. 6. EIS curves of the DSSCs with different photoanode and counter electrode, and the equivalent circuit for the DSSCs is shown as the inset.

3DGN. Therefore, the influence from the thickness of the 3DGN on the DSSCs was studied. The BET areas of the mono-, bi-, three- and multi-layer 3DGN are listed in Table S1, and the values decrease with increased thicknesses of the 3DGN due to the decreased ratio of the surface atoms. Moreover, the electrochemical properties of photoanode by using the 3DGN with varied thicknesses were analyzed by the photocurrent measurements. Under the identical condition (1 wt% 3DGNs were added into the photoanode), the photocurrent of the thinner (mono- and bi-layer) 3DGN modified photoanode is higher than that of the thicker (more than three-layer) 3DGN added sample, demonstrating the better electrochemical property of the former (Fig. 7a). Thereby, based on the results of BET area and photocurrent measurement, the thinner 3DGN assisted DSSCs should possess better photovoltaic performances. As expected, the η and J_{sc} decrease 7.5% and 5.6% when the thinner 3DGN was replaced by the thicker sample to add into the photoanode (see Fig. 7b and Table 2). Therefore, adopting thinner 3DGN can further improve the DSSCs performances.

Considering the excellently conductive property of the as-prepared 3DGN, a DSSC with the 3DGN based counter electrode was prepared (the photoanode was 3DGN (1 wt%)–P25, Fig. 8 displays the schematic image of the DSSC, SEM images of the electrodes are shown in the right side). The photovoltaic features of the resulted DSSC are listed in Table 1. Although the performance of the prepared DSSC is a bit worse than that by using a Pt counter

electrode, the resulted η is better than that of reported DSSCs with other carbon materials based counter electrode [8,15,38–42]. Compared to that of Pt counter electrode, there are several possible reasons which may lead to the degraded photovoltaic performance of the resulted DSSC: the poor catalytic property and stability of the 3DGN counter electrode, the poor conductive property of the 3DGN counter electrode or the contact between the 3DGN film and conductive glass is not good. The similar J_{sc} (15.4 mA cm^{-2} for the case of using Pt counter electrode and 14.6 mA cm^{-2} for using the 3DGN counter electrode) of the DSSCs indicates the excellent catalytic property of the 3DGN, while the high stability of the graphene as a counter electrode has been proven in previous reports [15,38,39]. The presence of the insulating adhesive (PTFE) increases the sheet resistance of the 3DGN from ~460 Ω sq^{-1} to ~1400 Ω sq^{-1}. However, the increased resistance is not the major reason for the degraded performance because the observed J_{sc} is still high. Although the DSSCs with the Pt and 3DGN counter electrodes show similar J_{sc}, the filling factor of the former is far higher, indicating that the poor contact between the 3DGN film and conductive glass is the reasonable explanation for the decreased η. In order to further prove the point, the EIS of the 3DGN counter electrode based DSSC was carried out (Fig. 6). The semicircle in the high frequency region of the DSSC is higher than that of the Pt counter electrode based sample, indicating that the interface contact impedance between the 3DGN film and conductive glass is larger than that of the Pt film and conductive glass. A good contact between Pt film and conductive glass forms during the high temperature process, while the combination of the 3DGN film and conductive glass only relies on the insulating binder. Cross-section SEM image shows that the structure of the 3DGN on the conductive glass is not compact (Fig. S9), indicating that the contact between the 3DGN film and the conductive glass cannot close enough. The reason is that the interaction between them is physical bonding rather than chemical bond. XPS results further confirm the conclusion because the 3DGNs before and after bonding to the conductive glass show identical C1s profile (more details see Supporting Information and Fig. S10).

Therefore, a further improvement of the DSSCs performance (with the 3DGN counter electrode) can be obtained after achieving a close contact between the 3DGN film and conductive glass, which is under study. Furthermore, the counter electrodes were also prepared by thinner and thicker 3DGNs to compare their performances. With the identical photoanode, the η of the DSSC by adopting the former based counter electrode is higher than using the latter (5.83% vs 5.72%). Therefore, both the photoanode and counter electrode display better performance when the thinner 3DGNs were employed.
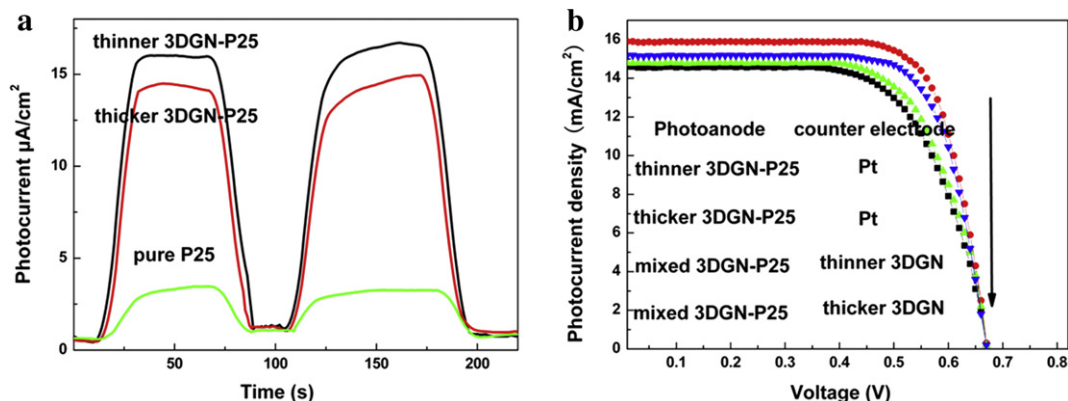

Fig. 7. (a) Photocurrents curves of different photoanodes, (b) J–V curves of the DSSCs with varied photoanode and counter electrode. All the amounts of the thinner, thicker and mixed 3DGN in the photoanodes are 1 wt%. The mixed 3DGN contains both the thinner and thicker 3DGN.

Table 2
Photovoltaic properties and dye loading of the DSSCs with varied photoanodes (thickness is 10 μm) and counter electrode. All measurements were recorded under AM-1.5G one sun and the active areas were ca. 0.15 cm^2 for all cells. All photoanodes include 1 wt% 3DGN, and the mixed 3DGN represent both the thinner and thicker samples are contained. The BET areas of the photoanode were listed.

Photoanodes (counter electrode)	J_{sc} (mA cm^{-2})	V_{oc} (mV)	FF (%)	η (%)	Absorbed dye ($\times 10^{-7}$ mol cm^{-2})	BET area (m^3 g^{-1})
Thinner 3DGN–P25 (Pt)	15.9	677	63.9	6.87	1.16	122.496
Thicker 3DGN–P25 (Pt)	15.0	672	63.1	6.36	1.15	114.127
Mixed 3DGN–P25 (thinner 3DGN–P25)	14.8	673	58.5	5.83	1.15	117.658
Mixed 3DGN–P25 (thicker 3DGN–P25)	14.6	674	58.1	5.72	1.15	117.658
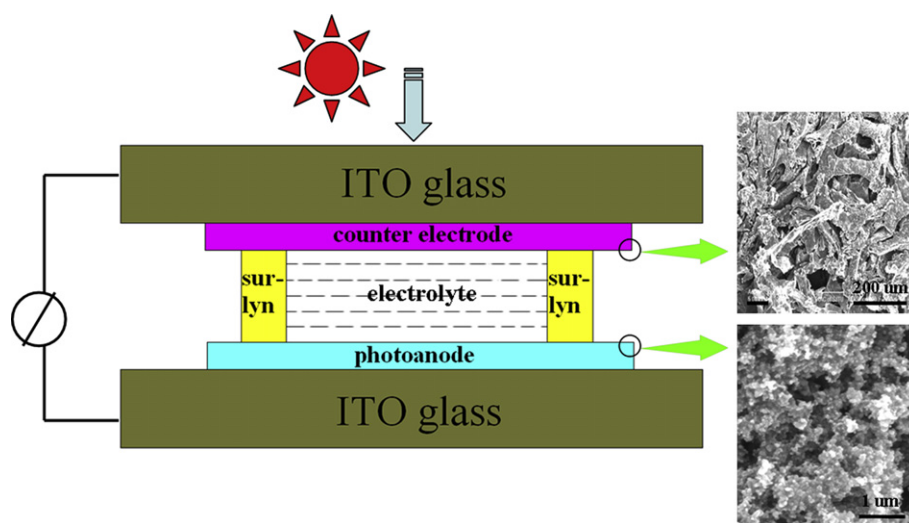
Fig. 8. Schematic image of the DSSC with 3DGN based photoanode and counter electrode, and the SEM images of the electrodes are displayed.

4. Conclusions

3DGN was fabricated by CVD with NFR as a template. The prepared sample possesses large BET area and outstanding electrical property, which are benefit for the dye absorption and electron transport abilities of the photoanode (as well as DSSCs performance). Moreover, the continuous structure between graphene sheets in the 3DGN provides a great transport channel for the photogenerated electrons from P25 to conductive glass. Obvious improvements in short circuit current density and power conversion efficiency of the DSSCs were observed by using the 3DGN modified photoanode. A η as high as 6.87% was obtained for the DSSC with a mono- and bi-layer 3DGN (1 wt%) included photoanode, in comparison with the 4.96% for the pristine P25 based sample. Moreover, DSSCs with the 3DGN based counter electrode and photoanode were also fabricated, and the resulted η up to 5.83%. Although Pt counter electrode based DSSC shows better performance, the further improvement for the 3DGN counter electrode based DSSC can be achieved by optimizing the contact between the 3DGN film and conductive glass.

Acknowledgments

Appendix A. Supplementary material

Supplementary material associated with this article can be found, in the online version, at http://dx.doi.org/10.1016/j. jpowsour.2013.01.130.

References

[1] B. Oregan, M. Gratzel, Nature 353 (1991) 737.
[2] B. Tang, G.X. Hu, J. Power Sources 220 (2012) 95.
[3] X. Wu, Q.G. Li, L.Z. Wang, Energy Environ. Sci. 4 (2011) 3565.
[4] W.J. Lin, C.T. Hsu, Y.C. Tsai, J. Colloid Interf. Sci. 15 (2011) 562.
[5] P. Brown, K. Takechi, P.V. Kamat, J. Phys. Chem. C 112 (2008) 4776.
[6] S.R. Sun, L. Gao, Y.Q. Liu, Appl. Phys. Lett. 96 (2010) 083113.
[7] C.Y. Liu, K.C. Huang, P.H. Chung, C.C. Wang, C.Y. Chen, R. Vittal, C.G. Wu, W.Y. Chiu, K.H. Ho, J. Power Sources 217 (2012) 152.
[8] S.I. Cha, B.K. Koo, S.H. Seo, D.Y. Lee, J. Mater. Chem. 20 (2010) 659.
[9] W.W. Sun, X.H. Sun, T. Peng, Y.M. Liu, H.W. Zhu, S.S. Guo, X.Z. Zhao, J. Power Sources 201 (2012) 402.
[10] H. Kim, H. Choi, S. Hwang, Y. Kim, M. Jeon, Nanoscale Res. Lett. 7 (2012) 53.
[11] J.G. Yu, J.J. Fan, B. Cheng, J. Power Sources 196 (2011) 7891.
[12] P. Dong, C.L. Pint, M. Hainey, F. Mirri, Y. Zhan, J. Zhang, M. Pasquali, R.H. Hauge, R. Verduzco, M. Jiang, H. Lin, J. Lou, ACS Appl. Mater. Interf. 3 (2011) 3157.
[13] K.S. Novoselov, A.K. Geim, S.V. Morozov, D. Jiang, Y. Zhang, S.V. Dubonos, I.V. Grigorieva, A.A. Firsov, Science 306 (2004) 666.
[14] T.H. Tsai, S.C. Chiou, S.M. Chen, Int. J. Electrochem. Sci. 6 (2011) 3333.
[15] H. Choi, H. Kim, S. Hwang, Y. Han, M. Jeon, J. Mater. Chem. 21 (2011) 7548.
[16] Z.P. Chen, W.C. Ren, L.B. Liu, S.F. Pei, H.M. Chen, Nat Mater. 10 (2011) 424.
[17] D.R. Dreyer, S.J. Park, W.C. Bielawski, R.S. Ruoff, Chem. Soc. Rev. 39 (2010) 228.
[18] Q.Q. Zhai, B. Tang, G.X. Hu, J. Hazard. Mater. 198 (2011) 78.
[19] K.S. Kim, Y. Zhao, H. Jang, S.Y. Lee, J.M. Kim, K.S. Kim, J.H. Ahn, P. Kim, J.Y. Choi, B.H. Hong, Nature 457 (2009) 706.
[20] B. Tang, G.X. Hu, H.Y. Gao, Appl. Spectrosc. Rev. 45 (2010) 369.
[21] A.C. Ferrari, J.C. Meyer, V. Scardaci, C. Casiraghi, K.S. Novoselov, A.K. Geim, Phys. Rev. Lett. 97 (2006) 187401.
[22] D. Graf, F. Molitor, Nano Lett. 7 (2007) 238.
[23] H.N. Zhen, Y. Ting, ACS Nano 3 (2009) 569.
[24] L. Wirtz, A. Rubio, Solid State Commun. 131 (2004) 141.
[25] A.C. Ferrari, Solid State Commun. 143 (2007) 47.
[26] C. Thomsen, S. Reich, Phys. Rev. Lett. 85 (2000) 5214.
[27] A. Gupta, G. Chen, P.C. Eklund, Nano Lett. 6 (2006) 2667.
[28] H. Hiura, T.W. Ebbesen, Chem. Phys. Lett. 202 (1993) 509.
[29] M.Y. Han, B. Oezylmaz, Y. Zhang, P. Kim, Phys. Rev. Lett. 98 (2007) 206805.
[30] B. Tang, G.X. Hu, M. Xia, Mater. Lett. 68 (2012) 104.
[31] B. Neumann, P. Bogdanoff, H. Tributsch, S. Sakthivel, H. Kisch, J. Phys. Chem. B 109 (2005) 16579.
[32] H. Zhang, X.J. Lv, Y.M. Li, Y. Wang, J.H. Li, ACS Nano 4 (2010) 380.

[33] Z.Z. Sun, Z. Yan, J. Yao, E. Beitler, Y. Zhu, J.M. Tour, Nature 468 (2010) 549.
[34] Y. Li, W.N. Wang, Z.L. Zhan, M. Woo, C.Y. Wu, P. Biswas, Appl. Catal. B: Environ. 100 (2010) 386.
[35] S. Ito, P. Liska, P. Comte, R.L. Charvet, P. Pechy, U. Bach, S.M. Zakeeruddin, A. Kay, M.K. Nazzerruddin, M. Gratezel, Chem. Commun. 41 (2005) 4351.
[36] L.Y. Lin, C.P. Lee, R. Vittal, K.C. Ho, J. Power Sources 195 (2010) 4344.
[37] C.P. Hsu, K.M. Lee, J.T.W. Huang, C.Y. Lin, C.H. Lee, L.P. Wang, S.Y. Tsai, K.C. Ho, Electrochim. Acta 53 (2008) 7514.
[38] S. Huang, H. Sun, X. Huang, Q. Zhang, D. Li, Y. Luo, Q. Meng, Nanoscale Res. Lett. 7 (2012) 222.
[39] S. Hwang, J. Moon, S. Lee, D.H. Kim, D. Lee, W. Choi, M. Jeon, Electron. Lett. 43 (2007) 25.
[40] G. Veerappan, W. Kwon, S.W. Rhee, J. Power Sources 196 (2011) 10798.
[41] K. Imoto, K. Takahashi, T. Yamaguchi, T. Komura, J. Nakamura, K. Murata, Sol. Energy Mater. Sol. C 79 (2003) 459.
[42] Q. Simone, G. Daniele, T. Mario, L. Laura, L. Alessandro, J. Power Sources 204 (2012) 249.